We are IntechOpen, the world's leading publisher of Open Access books Built by scientists, for scientists

6,900
Open access books available

185,000
International authors and editors

200M
Downloads

Our authors are among the

154
Countries delivered to

TOP 1%
most cited scientists

12.2%
Contributors from top 500 universities



WEB OF SCIENCE™

Selection of our books indexed in the Book Citation Index in Web of Science™ Core Collection (BKCI)

Interested in publishing with us?
Contact book.department@intechopen.com

Numbers displayed above are based on latest data collected.
For more information visit www.intechopen.com



3

Direct Numerical Simulation of Turbulence with Scalar Transfer Around Complex Geometries Using the Immersed Boundary Method and Fully Conservative Higher-Order Finite-Difference Schemes

Kouji Nagata[1], Hiroki Suzuki[1], Yasuhiko Sakai[1] and Toshiyuki Hayase[2]
[1]*Nagoya University*
[2]*Tohoku University*
Japan

1. Introduction

Direct numerical simulation (DNS) of turbulence is a powerful tool for the detailed investigation of a three-dimensional turbulent flow field, although the applications of DNS are currently restricted to moderate Reynolds numbers owing to limitations in computer resources. The numerical methods for DNS of turbulent flows are broadly categorized into the spectral method and finite difference method according to their numerical method (The finite element method is also used for coupling problems of fluid-structure interaction, but this method is beyond the scope of this chapter). The spectral method is highly accurate; however, owing to the numerical procedure involved, its application is limited to simple domains such as a cubic domain. On the other hand, the finite difference method can be applied to complex geometries, although its accuracy is generally lower than that of the spectral method. However, with recent developments in fully conservative higher-order finite-difference schemes (Morinishi et al. 1998), in the higher-order compact scheme originally developed for compressible flows (Lele 1992), and in the immersed boundary method for handling complex wall geometries (Fadlun et al. 2000; Ikeno & Kajishima 2007), DNS with spectral-like accuracy can be carried out around complex geometries with scalar transfer.

In this chapter, we demonstrate the method for performing DNS of incompressible turbulent flows with scalar transfer around complex geometries. In the first section, we present the results for the canonical channel flow with scalar transfer obtained using our DNS code and compare them with results obtained using the spectral method (Iwamoto et al. 2002; Kasagi et al. 1992). Then, we describe the numerical methods for the DNS of turbulent fields with scalar transfer around and downstream of regular and fractal grids (Hurst & Vassilicos 2007; Seoud & Vassilicos 2007; Mazellier & Vassilicos 2010) as an example of flow around complex geometries. The turbulence-generating grids are reproduced using the immersed boundary method (Fadlun 2000) with a direct forcing scheme in the Navier-Stokes equations. The fractional step method is employed for solving the governing equations. The use of

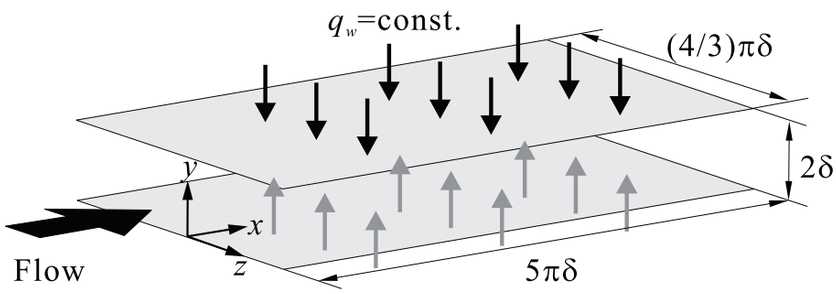


Fig. 1. Computational domain for the channel flow with scalar transfer (constant scalar flux condition)

the present method ensures a divergence-free condition up to machine accuracy ($\sim 10^{-14}$). Instantaneous flow fields and various turbulence quantities are presented and discussed. The method and results shown in this chapter pertain to state-of-the-art DNS of turbulence with scalar transfer around complex geometries based on the finite-difference method.

2. DNS of a channel flow with scalar transfer: validation of numerical technique

To validate our numerical simulation, we present the DNS results of a channel flow with scalar (heat) transfer. The results are compared with those obtained by the spectral method (Iwamoto et al. 2002; Kasagi et al. 1992).

2.1 Computational domain

Figure 1 shows the computational domain for the channel flow with scalar transfer (with a constant heat flux q_w). Table 1 lists the domain size (L_x, L_y, L_z), grid mesh points (N_x, N_y, N_z), and spatial resolutions ($\Delta_x^+, \Delta_y^+, \Delta_z^+$). The superscript $^+$ denotes the nondimensional quantities normalized by the inner parameters of the flow.
In the wall-normal y direction, we set the mesh points according to

$$y_i = 1 - \frac{\tanh\left[(2(1-2j/(N_y-1))\right]}{\tanh 2}, \ (j = 0 \sim N_y - 1) \tag{1}$$

to ensure spatial resolution near the wall.

	Present	Spectral (Iwamoto et al. 2002)	Spectral (Kasagi et al. 1992)
$L_x(L_x^+)$	$5\pi\delta$ (2,356)	$5\pi\delta$ (2,356)	$5\pi\delta$ (2,356)
$L_y(L_y^+)$	2δ (300)	2δ (300)	2δ (300)
$L_z(L_z^+)$	$(4/3)\pi\delta$ (942)	$2\pi\delta$ (628)	$2\pi\delta$ (628)
N_x	256	128	128
N_y	128	97	97
N_z	128	128	128
Δ_x^+	9.2	18.4	18.4
Δ_y^+	$0.35 \sim 4.86$	$0.08 \sim 4.9$	$0.08 \sim 4.9$
Δ_z^+	4.91	7.36	7.36
Re_τ	150	150	150
Pr	0.71	-	0.71

Table 1. Computational conditions

2.2 Governing equations

The governing equations are the incompressible Navier-Stokes equations (2), the continuity equation (3), and the transport equation for temperature fluctuations (4):

$$\frac{\partial U_i^+}{\partial t} + U_j^+ \frac{\partial U_i^+}{\partial x_j} = -\frac{\partial P^+}{\partial x_i} + \frac{1}{Re_\tau}\frac{\partial^2 U_i^+}{\partial x_j \partial x_j} + \frac{\partial P_w^+}{\partial x_i}\delta_{i1}, \tag{2}$$

$$\frac{\partial U_i^+}{\partial x_i} = 0, \tag{3}$$

$$\frac{\partial \theta^+}{\partial t} + U_j^+ \frac{\partial \theta^+}{\partial x_j} = \frac{1}{Re_\tau Pr}\frac{\partial^2 \theta^+}{\partial x_j \partial x_j} + U_1^+ \frac{\partial \overline{\langle T_m^+ \rangle}}{\partial x_1}, \tag{4}$$

where U_1, U_2, U_3 is U, V, W, (x_1, x_2, x_3) is (x, y, z) and the last term in Equation (2) is the streamwise mean pressure gradient to drive the flow. The equations are normalized using the inner parameters. $Re_\tau = u_\tau \delta / \nu$ is the friction Reynolds number and $Pr = \nu/\kappa$ is the Prandtl number (same as the Schmidt number Sc for scalar transfer); u_τ is the friction velocity, δ the half width of the channel (see Fig. 1), ν the kinematic viscosity, and κ the thermal diffusivity. In Equation (4), $\overline{\langle T_m^+ \rangle}$ is the mixed mean temperature averaged over the channel section, defined as (Kasagi et al. 1992)

$$\overline{\langle T_m^+ \rangle} = \int_0^{2\delta} \langle U_1^+ \rangle \langle T^+ \rangle \, dy \Big/ \int_0^{2\delta} \langle U_1^+ \rangle \, dy \,, \tag{5}$$

where T^+ is the instantaneous temperature normalized by the friction temperature T_τ ($= q_w/(\rho c_P u_\tau)$; ρ is the fluid density, c_P is the specific heat at constant pressure), and $\langle\ \rangle$ denotes the ensemble average.

2.3 Numerical methods

The fractional step method is employed for solving the governing equations. The Crank-Nicolson method is used for time-advancement of viscous and diffusion terms along y (wall-normal) direction, and the third-order Runge-Kutta method is used for the time advancement of other terms. The Poisson equation for pressure is solved using the diagonal matrix algorithm (DMA) along the vertical (y) direction and the fast Fourier transform (FFT) along the streamwise (x) and spanwise (z) directions. The Poisson equation is solved at each step of the Runge-Kutta method. In Equations (2) and (4), the pressure and convection terms along the x and z directions are discretized by the fully conservative 4th-order central scheme (CDS4) (Morinishi et al. 1998) and those along y direction are discretized by the fully conservative 2nd-order central scheme (CDS2) (Morinishi et al. 1998). Further, in these

	CCS4	CCS8
α	1/22	75/354
a	12/11	(37,950 - 39,275 α)/31,368
b	0	(65,115 α - 3,550)/20,912
c	0	(25,669 α - 6,114)/62,736
a_0	23/22	-

Table 2. Coefficients in the 4th- and 8th-order central compact scheme (CCS4 and CCS8) on a cell-centered mesh (Lele 1992)

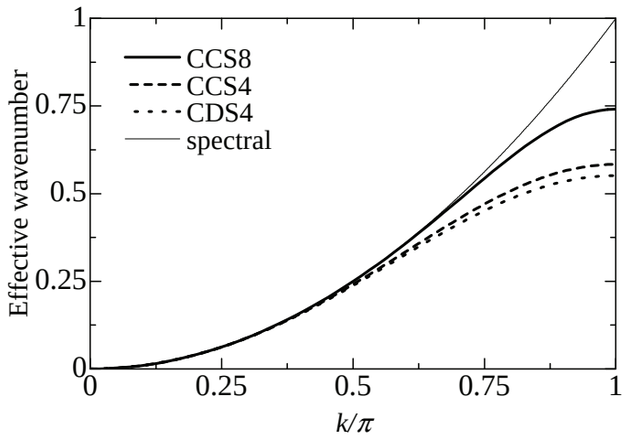


Fig. 2. Effective wavenumber for the cell-centered second derivative approximations (Lele 1992)

equations, the viscous and diffusion terms along the x and z directions are discretized by the 8th-order central compact scheme (CCS8) on a cell-centered mesh (Lele 1992) and those along the y direction are discretized by the 4th-order central compact scheme (CCS4) on a cell-centered mesh (Lele 1992). Here, the 4th- and 8th-order central compact scheme on a cell-centered mesh is expressed as

$$\alpha f'_{i-1} + f'_i + \alpha f'_{i+1} = a\frac{-f_{i-1/2} + f_{i+1/2}}{h} + b\frac{-f_{i-3/2} + f_{i+3/2}}{3h} + c\frac{-f_{i-5/2} + f_{i+5/2}}{5h}, \quad (6)$$

where f is a variable to be discretized; f', the derivative of f; $h(y)$, the width of the cell and is a function of y only. The coefficients are listed in Table 2. The truncation errors are $\left((9-62\alpha)/1{,}920\right)h^4 f^{(5)}$ for CCS4 and $\left((96{,}850-288{,}529\alpha)/1{,}686{,}343{,}680\right)h^8 f^{(9)}$ for CCS8 (Lele 1992). At the solid surface, the following discretization is used:

$$f'_i + \alpha f'_{i+1} = a_0\frac{-f_{i-1/2} + f_{i+1/2}}{h}. \quad (7)$$

The second derivative of f is also calculated using Equation (6). Figure 2 shows the effective (or modified) wavenumber (Lele 1992) for the cell-centered second derivative approximations. Figure 2 shows that compact schemes (CCS4 and CCS8) provide accurate results up to the high wavenumber region.

In our code, the compact schemes are used only for the diffusion and viscous terms since the energy and mass conservations at the wall have not been comprehensively discussed for the compact scheme applied to nonlinear terms. In addition, the application of the compact scheme to nonlinear terms requires an iterative method for solving the Poisson equation, resulting in a huge computational cost. It should be noted that the viscous effect is considered an important factor in the behavior at the near-wall region and when evaluating spectra in high wavenumber regions.

Using the above schemes, the divergence-free condition is ensured up to the machine accuracy ($\sim 10^{-14}$). Simulations were carried out using the NEC SX-8 supercomputer at the Advanced Fluid Information Research Center, Institute of Fluid Science, Tohoku University. The vectorization ratio is 99.7%. The effective performance is 13 GFLOPS and this value corresponds to approximately 81% of the theoretical performance of 16.0 GFLOPS. These results indicate that our code has been highly optimized.

2.4 Flow conditions

The friction Reynolds number Re_τ is 150, which is the same value as that used in Iwamoto et al. (2002) and Kasagi et al. (1992). The uniform heat flux condition (same as in Kasagi et al. 1992) is applied to the lower and upper walls. The Prandtl number is set at $Pr = 0.71$, considering heat transfer in an air flow.

2.5 Results and discussions

2.5.1 Flow field

Figure 3 shows the vertical ($y^+ = yu_\tau/\nu$) profiles of mean velocity and rms values of velocity fluctuations normalized by u_τ. Figure 4 shows the vertical profiles of the Reynolds shear stress normalized by u_τ^2. These profiles indicate that our results are in good agreement with those obtained using the spectral method.

Figure 5 shows the vertical profiles of various terms in the transport equation for the Reynolds stress. Using the notation of the Einstein summation convention for index k, the transport equation can be expressed as

$$\frac{D\left\langle u_i^+ u_j^+ \right\rangle}{Dt} = P_{ij} + T_{ij} + \Pi_{ij} + D_{ij} - \varepsilon_{ij}, \tag{8}$$

$$P_{ij} = -\left\langle u_j^+ u_k^+ \right\rangle \frac{\partial U_i^+}{\partial x_k^+} - \left\langle u_i^+ u_k^+ \right\rangle \frac{\partial U_j^+}{\partial x_k^+}, \tag{9}$$

$$T_{ij} = -\frac{\partial \left\langle u_i^+ u_j^+ u_k^+ \right\rangle}{\partial x_k^+}, \tag{10}$$

$$\Pi_{ij} = -\left\langle u_j^+ \frac{\partial p^+}{\partial x_i^+} \right\rangle - \left\langle u_i^+ \frac{\partial p^+}{\partial x_j^+} \right\rangle, \tag{11}$$

$$D_{ij} = \frac{\partial^2 \left\langle u_i^+ u_j^+ \right\rangle}{\partial x_k^+ \partial x_k^+}, \tag{12}$$

$$\varepsilon_{ij} = 2\left\langle \frac{\partial u_i^+}{\partial x_k^+} \frac{\partial u_i^+}{\partial x_k^+} \right\rangle, \tag{13}$$

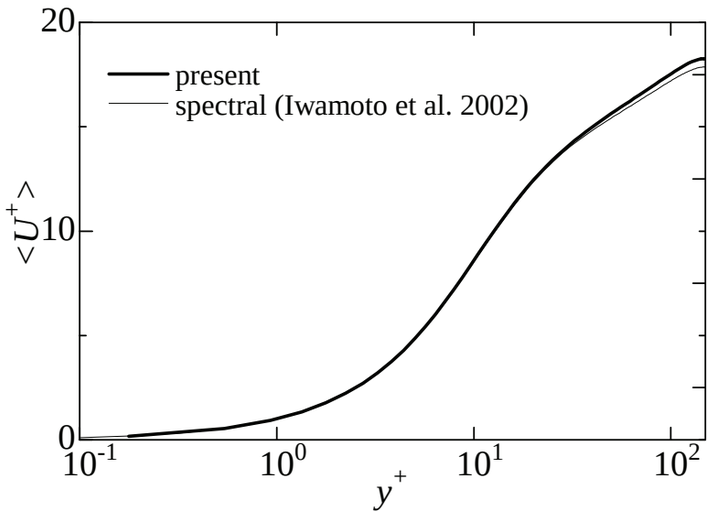
where $U_i^+ = \langle U_i^+ \rangle + u_i^+$ and $P^+ = \langle P^+ \rangle + p^+$. Π_{ij} can be divided into the pressure-diffusion term Ψ_{ij} and pressure-strain term Φ_{ij}:

$$\Pi_{ij} = \Psi_{ij} + \Phi_{ij}, \tag{14}$$

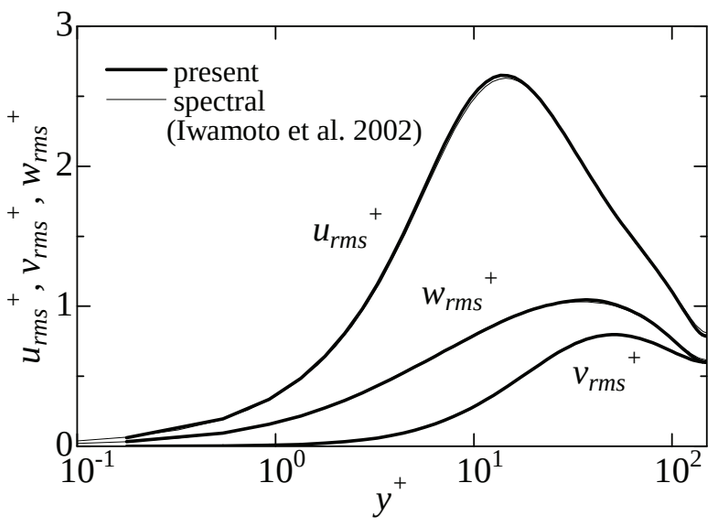
$$\Psi_{ij} = -\left\langle \frac{\partial (u_j^+ p^+)}{\partial x_i^+} \right\rangle - \left\langle \frac{\partial (u_i^+ p^+)}{\partial x_j^+} \right\rangle, \tag{15}$$

$$\Phi_{ij} = \left\langle p^+ \frac{\partial u_j^+}{\partial x_i^+} \right\rangle + \left\langle p^+ \frac{\partial u_i^+}{\partial x_j^+} \right\rangle. \tag{16}$$

Figure 5 shows that our results are in good agreement with those obtained using the spectral method.



(a) Mean velocity



(b) Rms of velocity fluctuations

Fig. 3. Vertical profiles of mean and rms values

Figure 6 shows the dissipation spectra of u_i^+, $(k_z\delta)^2 E_{u_i u_i}$, and cospectra of $\langle u^+ v^+ \rangle$, E_{uv}, evaluated at $y^+ = 15$. It can be observed that up to the high-frequency range, our results are in good agreement with those obtained using the spectral method.

2.5.2 Scalar field

Owing to space restrictions, only four profiles are presented here. Figure 7 shows the vertical profiles of mean temperature $\langle T^+ \rangle$ and temperature variance $k_\theta^+ = \frac{1}{2}\langle \theta^{+2} \rangle$, normalized using T_τ. Figure 7 shows that our results are in good agreement with those obtained using the spectral method.

Figure 8 shows the vertical profiles of $-\phi_{v\theta}$ and $-\psi_{v\theta}$ in the transport equation for vertical turbulent heat flux $-\langle v^+ \theta^+ \rangle$:

$$-\phi_{v\theta} = \left\langle p^+ \frac{\partial \theta^+}{\partial y^+} \right\rangle, \tag{17}$$

$$-\psi_{v\theta} = -\frac{\partial \langle p^+ \theta^+ \rangle}{\partial y^+}. \tag{18}$$

In general, the computational errors of these terms are larger than those of the other terms. Figure 8 shows that our results are in good agreement with those obtained using the spectral method. We have also confirmed that other statistics on scalar quantities (not shown here) are in good agreements with those obtained using the spectral method.

These results on turbulent and scalar fields indicate that the accuracy of our code is comparable to that of the spectral code. In the next section, we will show the computational results for grid turbulence with scalar transfer as an example of flow around complex geometries. The code employed is based on the code presented in this section, along with the immersed boundary method for handling complex wall geometries (Fadlun et al. 2000).

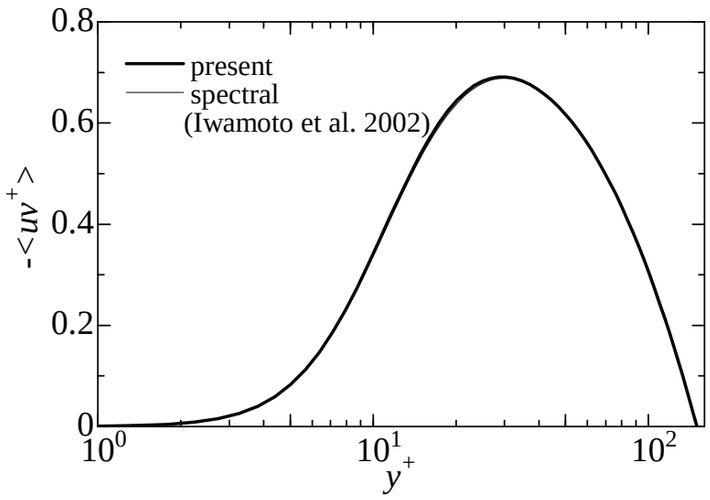
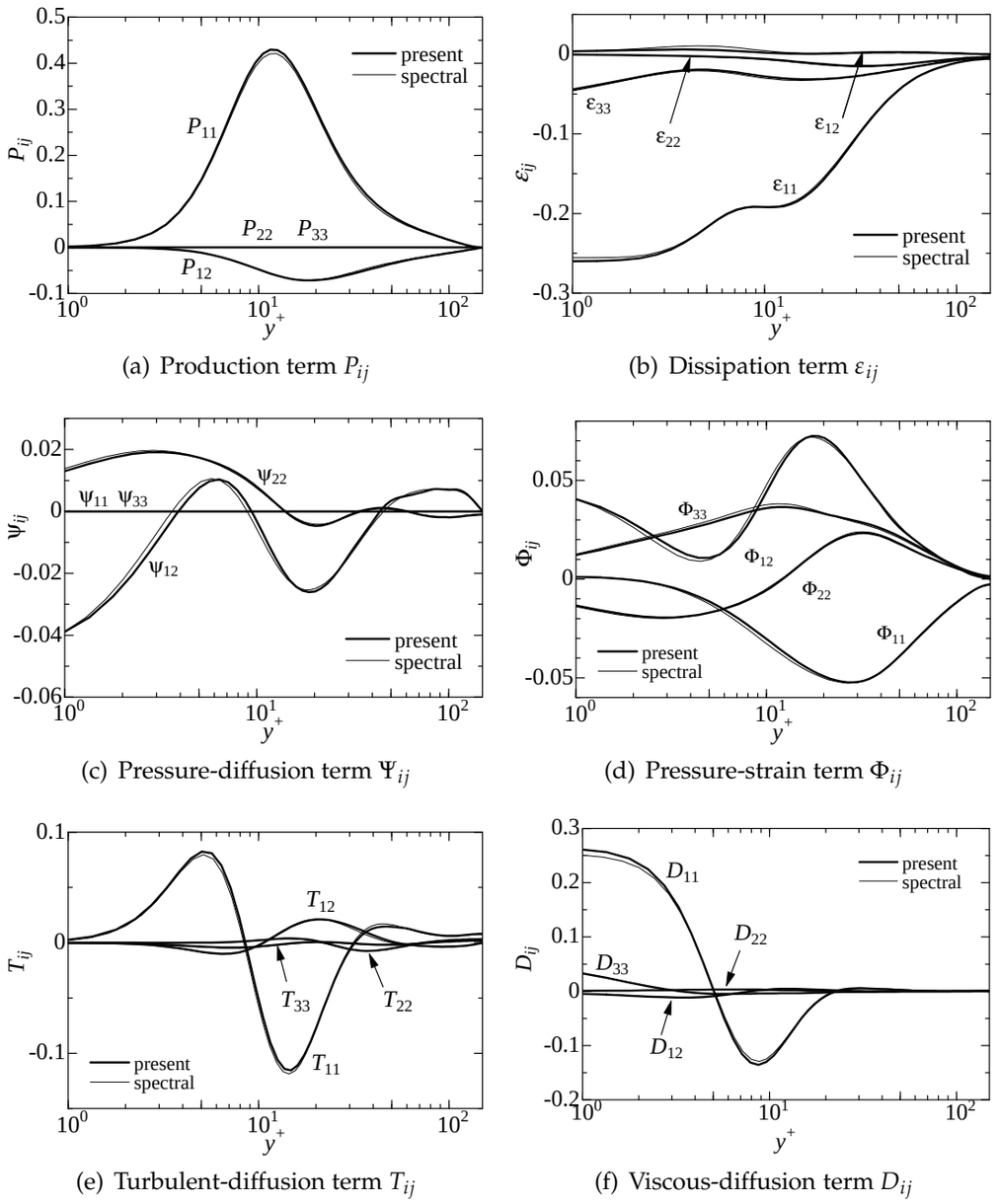


Fig. 4. Vertical profiles of Reynolds shear stress

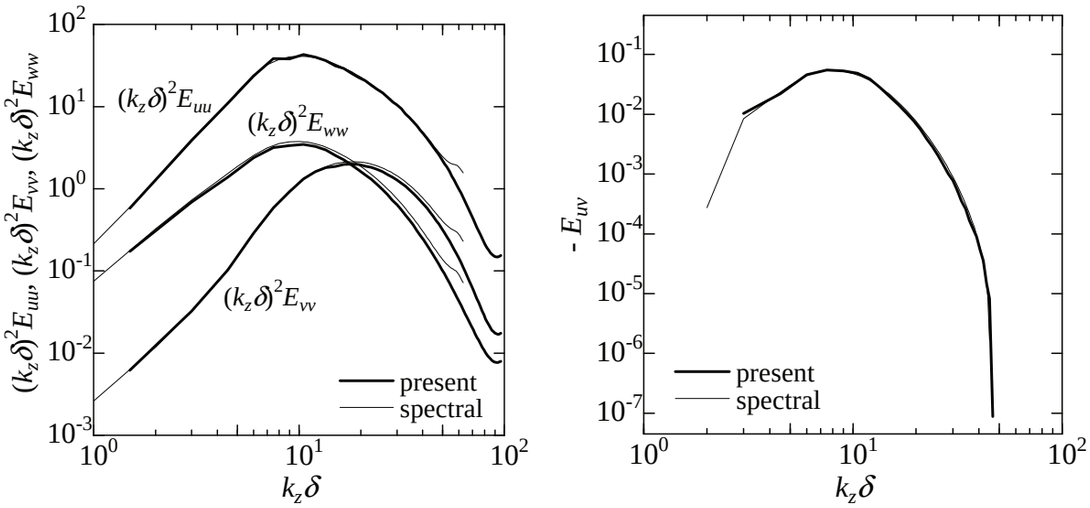


(a) Production term P_{ij} (b) Dissipation term ε_{ij}

(c) Pressure-diffusion term Ψ_{ij} (d) Pressure-strain term Φ_{ij}

(e) Turbulent-diffusion term T_{ij} (f) Viscous-diffusion term D_{ij}

Fig. 5. Vertical profiles of various terms in the transport equation for the Reynolds stress



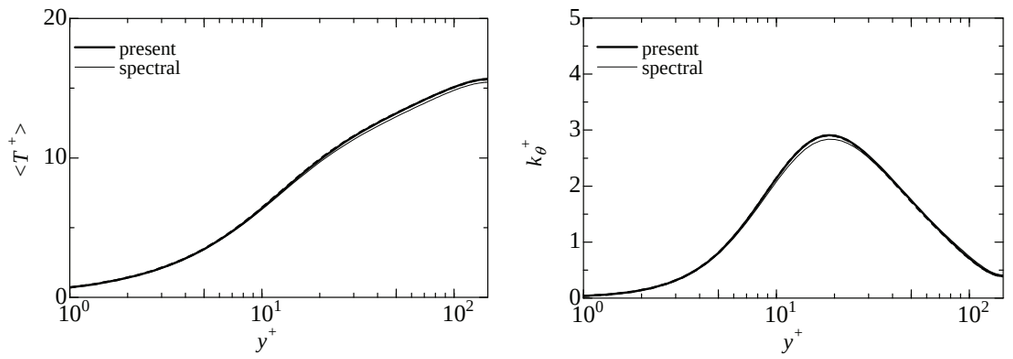
(a) Dissipation spectra (b) Cospectra of $\langle u^+v^+ \rangle$

Fig. 6. Dissipation spectra and cospectra at $y^+ = 15$

3. DNS of grid-generated turbulence: an example of flow around complex geometries

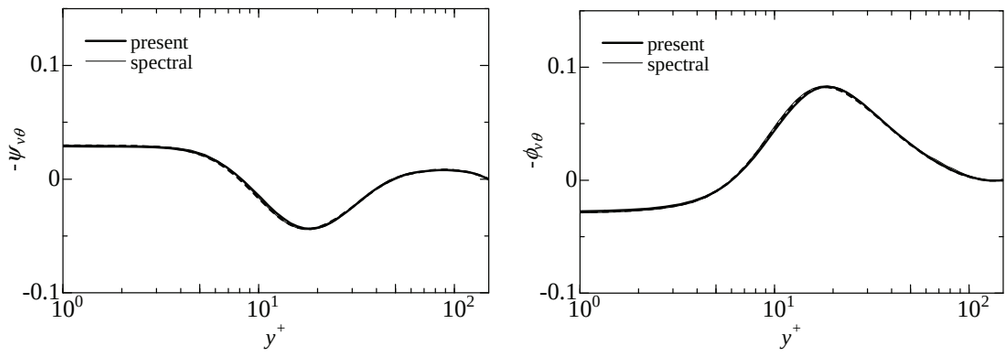
3.1 Background

Grid-generated turbulence has been widely used to generate quasi-isotropic turbulence in wind tunnels and water channels and has been applied to investigate the heat transfer in a wind tunnel (Warhaft & Lumley 1978; Sreenivasan et al. 1980; Budwig et al. 1985), mass transfer in a water channel (Huq & Britter 1995), scalar diffusion from line and point sources (Stapountzis et al. 1986; Nakamura et al. 1987), turbulent transport of small particles in a wind tunnel (Gad-el-Hak & Morton 1979), heat and mass transfer in stable density stratification (Stillinger et al. 1983; Lienhard & Van Atta 1990; Jayesh et al. 1991; Komori & Nagata 1996; Nagata & Komori 2001), mass transfer in unstable density stratification (Nagata & Komori 2000), and mass transfer with a chemical reaction (Komori et al. 1993; Nagata & Komori 2000; Ito et al. 2002). Grid-generated turbulence is also considered in turbulence analysis (Nagata et al. 2006, 2010).



(a) Mean temperature (b) Temperature variance

Fig. 7. Vertical profiles of mean temperature and temperature variance



(a) Pressure temperature-gradient term $-\phi_{v\theta}$

(b) Pressure-diffusion term $-\psi_{v\theta}$

Fig. 8. Vertical profiles of $-\phi_{v\theta}$ and $-\psi_{v\theta}$ in the transport equation for vertical turbulent heat flux $-\langle v^+\theta^+\rangle$

However, it is very difficult to completely understand the turbulence and scalar fields in the aforementioned flows through conventional measurements using hot wire/film probes or laser Doppler velocimetry for velocity field and using a cold-wire or electrode-conductivity probes (e.g., Gibson & Schwarz 1963) or laser induced fluorescence (LIF) technique for scalar field. For instance, the direct measurement of fundamental statistics such as those including pressure fluctuation and/or spatial derivatives is difficult; these statistics are usually estimated from limited measurable quantities using certain hypotheses. Recently, the measurements of grid-generated turbulence have been conducted using particle image velocimetry (PIV) (Proud et al. 2005; Suzuki et al. 2010a), and more detailed information on the flow field has been obtained. However, it is still difficult to elucidate three-dimensional structures in the aforementioned flows.

Recently, turbulence generated by the fractal grid has also been investigated in previous studies (Hurst & Vassilicos 2007; Seoud & Vassilicos 2007; Mazellier & Vassilicos 2010). These studies showed that fractal grids generate unusually high turbulence intensities and that fractal forcing by the fractal grids modifies turbulence so greatly that the dissipation, spectra, and evolution of integral and Taylor microscales exhibit considerably unusual behaviors. To completely understand these new types of turbulence generated by fractal grids, information on the three-dimensional flow field is required.

DNS of the grid-generated turbulence is the most suitable approach for addressing these issues, although the application of DNS to complex geometry is currently limited to low to moderate Reynolds numbers. It should be noted that the Reynolds numbers in some

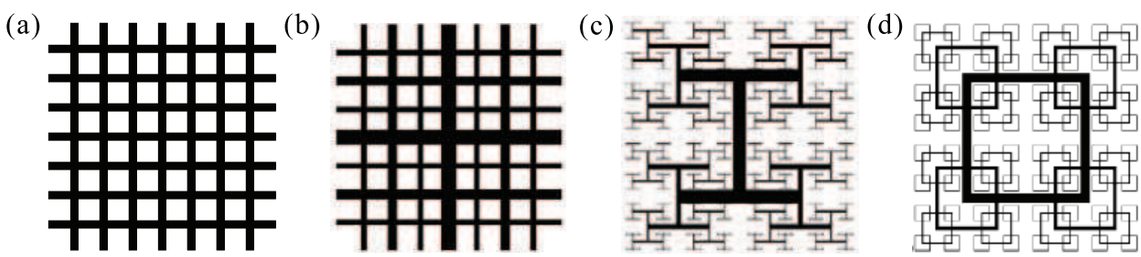


Fig. 9. Schematics of the turbulence-generating grids: (a) regular grid; (b) fractal cross grid; (c) fractal I grid; (d) fractal square grid (after Hurst & Vassilicos 2007)

Grid type	D_f	N	σ	t_r
Regular	2.0	1	0.36	1
Fractal I	2.0	4	0.36	8.5
Fractal cross	2.0	4	0.36	8.5
Fractal square	2.0	4	0.36, 0.44	5.0, 8.5, 13.0, 15.0

Table 3. Specifications of the turbulence-generating grids

important flows (e.g., Nagata & Komori 2000, 2001; Ito et al. 2002) are not very large. Since future advancements in supercomputers can be anticipated fairly confidently, it can be assumed that DNS of complex geometry at high Reynolds numbers should soon become possible.
In this section, we describe the numerical method for performing DNS of grid-generated turbulence with scalar transfer. The DNS code for fractal grid turbulence has also been independently developed by Laizet & Vassilicos (2010) using a different approach. The numerical code is applied to DNS of a turbulent field with scalar transfer downstream of regular and fractal grids, and the characteristics of flow and scalar fields are presented.

3.2 Turbulence-generating grids

Figure 9 shows the schematics of turbulence-generating regular and fractal grids. The regular grid consists of a square bar, square mesh, and biplane construction. In the present DNS, all bars of the fractal grid have square cross-sections, although all these bars have the same thickness in the direction of a mean flow in the previous experiments (Hurst & Vassilicos 2007; Seoud & Vassilicos 2007; Mazellier & Vassilicos 2010). The grid parameters are listed in Table 3. Here, D_f is the fractal dimension; N, the fractal iteration; σ, the solidity; and t_r, the thickness ratio of the largest bar thickness to the smallest bar thickness, t_{max}/t_{min}. The values of D_f and N for the fractal grids are the same as those used in previous experiments (Hurst & Vassilicos 2007; Seoud & Vassilicos 2007; Mazellier & Vassilicos 2010). Details on the fractal grids are provided in Hurst & Vassilicos (2007).

3.3 Computational domain

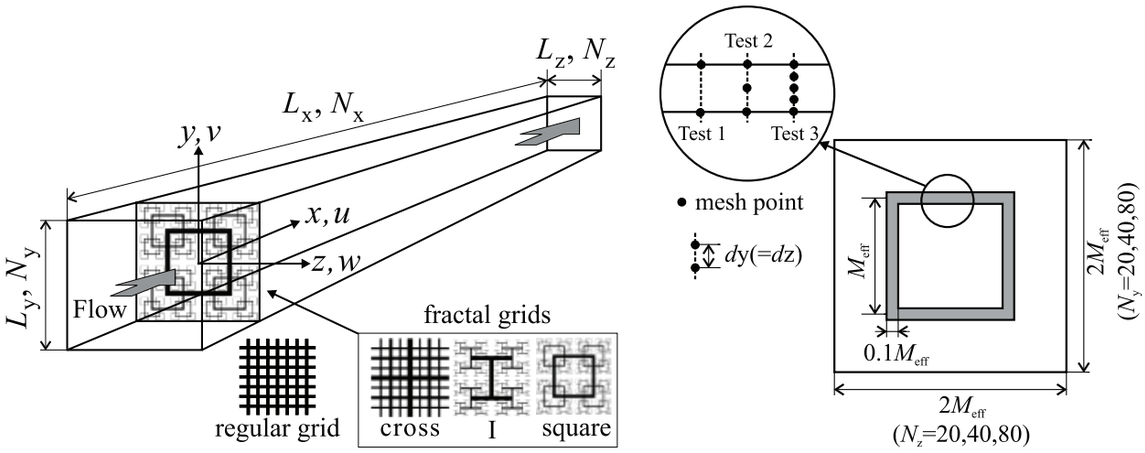
Figure 10 shows the computational domain. Here, L_x,L_y, and L_z are normalized by the effective mesh size, M_{eff} (refer to Hurst & Vassilicos 2007 for further details on M_{eff}). The domain size and number of mesh points are listed in Table 4. The turbulence-generating grid is numerically constructed at $5M_{eff}$ downstream from the entrance. In runs Tests $1 \sim 3$, only the smallest grid (the smallest component of the fractal grid) is placed in the middle of the domain at $x/M_{eff} = 0$, as shown in Fig. 10 (b), to determine the minimum number of mesh points in the y or z direction for reproducing the suitable wakes of the smallest grid bars. The domain size for runs Tests $1 \sim 3$ is $2M_{eff} \times 2M_{eff}$ in cross section (which corresponds to $(1/8)^2$ of that for the actual fractal grids, i.e., runs SFG1$\sim$3, SFGm1$\sim$3). The length and thickness of the smallest bar used in runs Tests $1 \sim 3$ are M_{eff} and $0.1M_{eff}$, respectively. In run Test 1, only two mesh points are arranged on the bar in the y or z direction. In runs Tests 2 and 3, three and five mesh points, respectively, are arranged on the bar in the y or z direction. Note that more mesh points (which are identical for all runs) are arranged on the bar in the streamwise (x) direction as shown in section 3.5.2. The number of mesh points for other runs are determined after performing runs Tests $1 \sim 3$. The dependence of mesh points on the wakes is discussed in section 3.8.1.

Run	grid	L_x	L_y, L_z	N_x	N_y, N_z	Re_M	Pr
Test1	Fractal square ($N = 1$)	38.4	2	512	20	2,500	-
Test2	Fractal square ($N = 1$)	38.4	2	512	40	2,500	-
Test3	Fractal square ($N = 1$)	38.4	2	512	80	2,500	-
RG1	Regular (S_θ =const)	115.2	8	1,280	160	2,500	0.71
RGm1	Regular (s.m.l.)	64.0	8	768	160	2,500	0.71
CFG	Fractal cross	115.2	16	1,280	320	2,500	-
IFG	Fractal I	115.2	16	1,280	320	2,500	-
SFG1	Fractal square (S_θ =const) ($t_r = 8.5, \sigma = 0.36$)	115.2	16	1,280	320	2,500	0.71
SFG2	Fractal square ($t_r = 15.0, \sigma = 0.36$)	115.2	16	1,280	416	2,500	-
SFG3	Fractal square ($t_r = 8.5, \sigma = 0.44$)	115.2	16	1,280	256	2,500	-
SFGm1	Fractal square ($t_r = 5.0, \sigma = 0.36$, s.m.l.)	64.0	16	768	256	2,500	0.71
SFGm2	Fractal square ($t_r = 8.5, \sigma = 0.36$, s.m.l.)	64.0	16	768	320	2,500	0.71
SFGm3	Fractal square ($t_r = 13.0, \sigma = 0.36$, s.m.l.)	64.0	16	768	416	2,500	0.71

Table 4. Computational conditions. (s.m.l.: scalar mixing layer)

3.4 Governing equations

The governing equations are the forced incompressible Navier-Stokes equations (19), the continuity equation (20), the forced transport equation for scalar fluctuations (21) in case of the linear scalar gradient, and the forced transport equation for instantaneous scalar (22) in case of the scalar mixing layer:



(a) For runs RG, IFG, CFG and SFG

(b) Schematic of the cross-section at $x = 0$ of the computational domain for runs Tests $1 \sim 3$. The cross-sectional area is $(1/8)^2$ of that for run SFG

Fig. 10. Schematic of computational domain

$$\frac{\partial U_i}{\partial t} + U_j \frac{\partial U_i}{\partial X_j} = -\frac{\partial P}{\partial X_i} + \frac{1}{Re_M} \frac{\partial^2 U_i}{\partial X_j \partial X_j} + F_i, \tag{19}$$

$$\frac{\partial U_i}{\partial X_i} = 0, \tag{20}$$

$$\frac{\partial \theta}{\partial t} + U_j \frac{\partial \theta}{\partial X_j} + U_2 S_\theta = \frac{1}{Re_M Pr} \frac{\partial^2 \theta}{\partial X_j \partial X_j} + F_\theta, \tag{21}$$

$$\frac{\partial T}{\partial t} + U_j \frac{\partial T}{\partial X_j} = \frac{1}{Re_M Pr} \frac{\partial^2 T}{\partial X_j \partial X_j} + F_T, \tag{22}$$

where S_θ is the constant scalar gradient. The equations are normalized using U_0, M_{eff}, and the characteristic value of scalar ΔT. Here ΔT is chosen as the scalar difference within the vertical length M_{eff} in case of the linear scalar gradient and is chosen as the scalar difference between the upper and lower streams in case of the scalar mixing layer. In Equations (19) and (21), the force terms, F_i, F_θ, and F_T, are introduced for satisfying the boundary conditions on the grid surface when using the immersed boundary method (Fadlun et al. 2000).

3.5 Boundary conditions

3.5.1 Boundary conditions at the boundary of domain

The uniform flow U_0 is given as an inflow, in which no velocity or scalar fluctuations are provided. The periodic boundary conditions are imposed for all variables in the vertical and spanwise directions. The convective outflow condition:

$$\frac{\partial \beta}{\partial t} + U_c \frac{\partial \beta}{\partial X_1} = 0, \tag{23}$$

is applied for velocities and scalar at the exit, where β denotes the instantaneous velocity or instantaneous scalar or scalar fluctuation, and U_c denotes the convection velocity, which is set equal to U_0. For pressure, the Neumann condition is applied at the inlet and the Dirichlet-Neumann condition is applied at the exit.

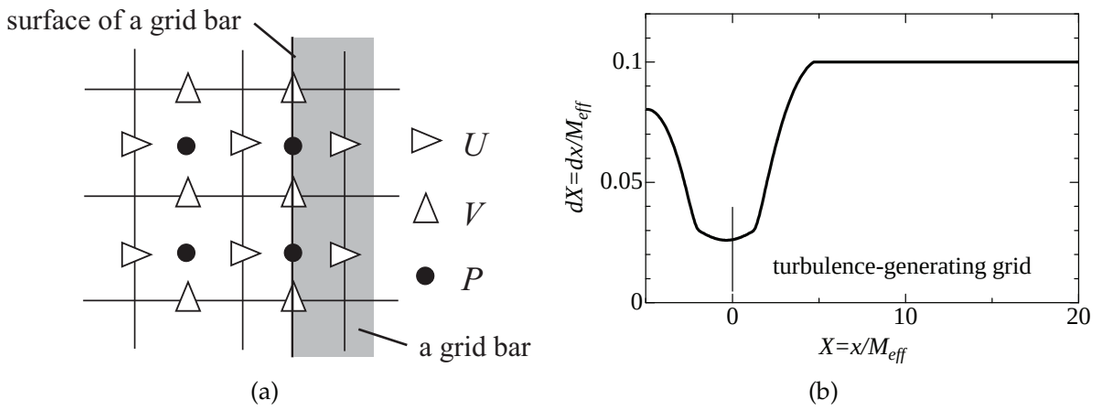


Fig. 11. (a) Schematic of surface layout and (b) streamwise variation of streamwise mesh size dX

3.5.2 Boundary conditions on the grid surface

The immersed boundary method (Fadlun et al. 2000) is used to satisfy the boundary conditions on the grid surface. This method employs the force term F_i to satisfy the specified Dirichlet conditions on the solid surface. The direct forcing method (Fadlun et al. 2000) has been adopted in the present DNS. To solve Equations (19) and (20) using the fractional step method, the Poisson equation should be solved. Ikeno & Kajishima (2007) stated that existing schemes for the immersed boundary method violate the wall condition during time advancement due to the inconsistency between the pressure and the velocity interpolated to represent the solid wall; they developed a modified pressure equation based on the interpolated pressure gradient. However, in this method, an iterative process is required to solve the Poisson equation, which requires extensive computational resources. Fortunately, turbulence-generating grids have surfaces parallel and perpendicular to the Cartesian grid system; therefore, we reduced the pressure inconsistency problem by adopting the mesh arrangement shown in Fig. 11 (a). Since the definition points of the pressure exist on the grid surface, the pressure does not require interpolation, and can be directly determined from the Poisson equation. Most definition points for the velocities are also arranged on the grid surface to directly specify the nonslip wall conditions. The staggered mesh arrangement is used in this study to prevent spurious pressure oscillations.

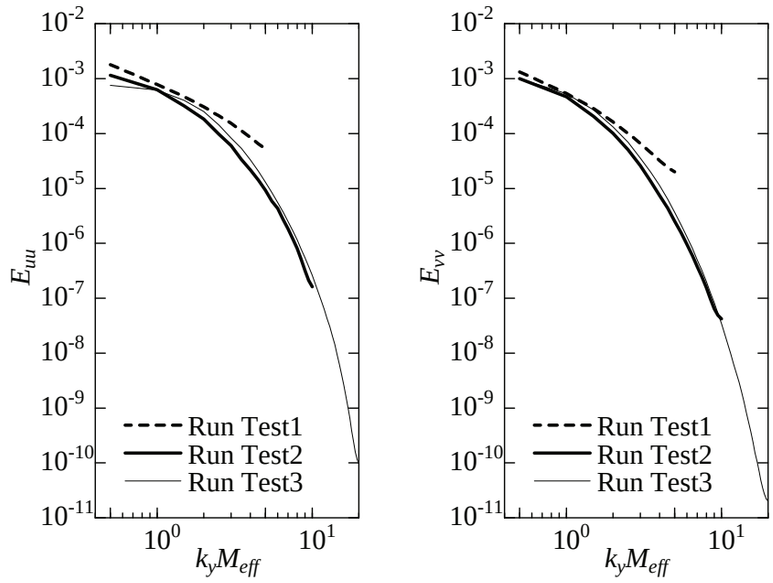
With these mesh arrangements for the grid surface, we can reproduce suitable wakes behind the smallest bars. It should be noted that suitable wakes were not reproduced when other mesh arrangements were used for the present mesh sizes (spatial resolutions) and Reynolds number. In addition, spatial resolutions around the turbulence-generating grids were ensured by concentrating the grid points in the streamwise (x) direction, as shown in Fig. 11 (b). This grid system is used for all runs listed in Table 4. Around the turbulence-generating grid, dX is about $1/4$ of the far downstream value. These mesh arrangements prevent numerical instability around the grid bars. It should be noted that numerical filters and non-physical numerical viscosity, which are often used to prevent numerical instability, were not used in the present DNS.

3.6 Numerical methods

The numerical methods used here are similar to those described in section 2, with some modifications as described below. The third-order Runge-Kutta method is used for time advancement. The Poisson equation for pressure is solved using the diagonal matrix algorithm (DMA) along the streamwise (x) direction and the fast Fourier transform (FFT) along the vertical (y) and spanwise (z) directions. The pressure and convection terms along the y and z directions in Equations (19) and (21) are discretized by the fully conservative 4th-order central scheme (CDS4) (Morinishi et al. 1998), and those along the x direction, by the fully conservative 6th-order central scheme (CDS6) (Morinishi et al. 1998). The viscous and diffusion terms along the y and z directions in Equations (19) and (21) are calculated by the Fourier spectral method, and those along the x direction are discretized by the 8th-order central compact scheme (CCS8) on a cell-centered mesh (Lele 1992).

3.7 Flow conditions

The mesh Reynolds number $Re_M (= U_0 M_{eff}/\nu)$ is set at 2,500 for all cases. This value is much smaller than that used in previous experiments on fractal grid turbulence (Hurst & Vassilicos 2007; Seoud & Vassilicos 2007; Mazellier & Vassilicos 2010) owing to limitations in computer resources; however, it is the same as that used in Komori & Nagata (1996) and



(a) Energy spectra of u (b) Energy spectra of v

Fig. 12. Energy spectra of u and v at $x/M_{eff} = 8$ for runs Tests $1 \sim 3$. In runs Tests $1 \sim 3$, two, three, and five mesh points are respectively arranged on the bar in the y or z direction

Nagata & Komori (2000, 2001). For a linear scalar gradient (runs RG1 and SFG1), the constant scalar gradient S_θ is set to $1/16$ for both regular and fractal grid turbulence. Therefore, the normalized maximum scalar difference in the vertical direction is 1.0 for the fractal grid turbulence (run SFG1) and is $1/2$ for the regular grid turbulence (run RG1). For a scalar mixing layer (runs RGm1 and SFGm1 $\sim$ SFGm3), the initial nondimensional scalar is $T = 1$ and $T = 0$ in the upper and lower half streams, respectively. Therefore, scalar mixing layers that initially have a step profile develop downstream of the grids, as in the previous experiments (e.g. Huq & Britter 1995; Komori & Nagata 1996; Nagata & Komori 2000, 2001; Suzuki et al. 2010a). The Prandtl number Pr is set at 0.71, considering heat transfer in an air flow. It should be noted that it is impossible to perform DNS of high-Schmidt-number scalar fields because the smallest scale of the scalar field (i.e., the Batchelor scale), $\eta/\sqrt{\mathrm{Sc}}$, is considerably small at a high Schmidt number; here, η is the Kolmogorov scale and Sc is the Schmidt number ($\mathrm{Sc} \approx 2{,}100$ in our previous experiments using Rhodamine B (Suzuki et al. 2010a)).

3.8 Results and discussions

3.8.1 Grid dependence on wakes of grid bars

Figure 12 shows the energy spectra of u and v at $x/M_{eff} = 8$ for runs Tests $1 \sim 3$. In run Test 1, the spectra obviously differ from those for runs Tests 2 and 3. Therefore, at least three mesh points should be arranged in the vertical (or spanwise) direction to accurately reproduce the wakes of the smallest grid bars. It should be noted that this result is for the smallest bars (corresponding to $j = N - 1 = 3$ in runs CFG, IFG, SFG1 $\sim$ 3, and SFGm1 $\sim$ 3) of the actual fractal grid; naturally, more mesh points are arranged on the larger bars for iterations of $j = 0$ (the largest component of the fractal grid) $\sim$ 2 (the second smallest component of the fractal grid). In addition, the results depended on the resolution of time advancement as well as the number of mesh points: proper wakes were not reproduced when the 2nd and 3rd order Adams-Bashforth schemes were employed.

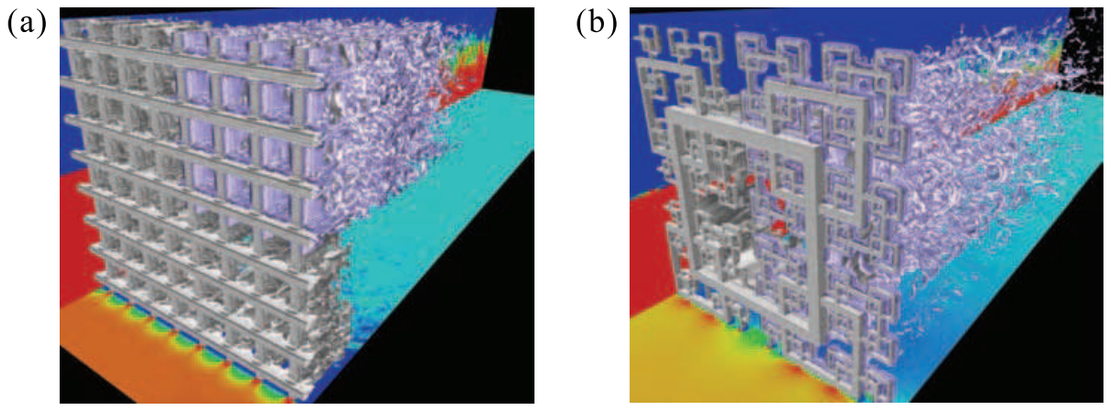


Fig. 13. Instantaneous flow fields around turbulence-generating grids: (a) regular grid (run RGm1); (b) fractal square grid (run SFGm2)

3.8.2 Instantaneous and mean flow fields

Figure 13 shows the snapshots of the instantaneous flow fields near the grids. The grid is visualized using the isovelocity surface in case of instantaneous streamwise velocity $U = 0$. The isosurfaces of the second invariant of the velocity gradient tensor Q, contour of pressure P (on the bottom plane near $y = -8M_{eff}$), and contour of scalar for the mixing layer (on the side plane near $z = -8M_{eff}$) are drawn. Here, Q is defined as

$$Q = \frac{1}{2}\left(W_{ij}W_{ij} - S_{ij}S_{ij}\right), \tag{24}$$

where,

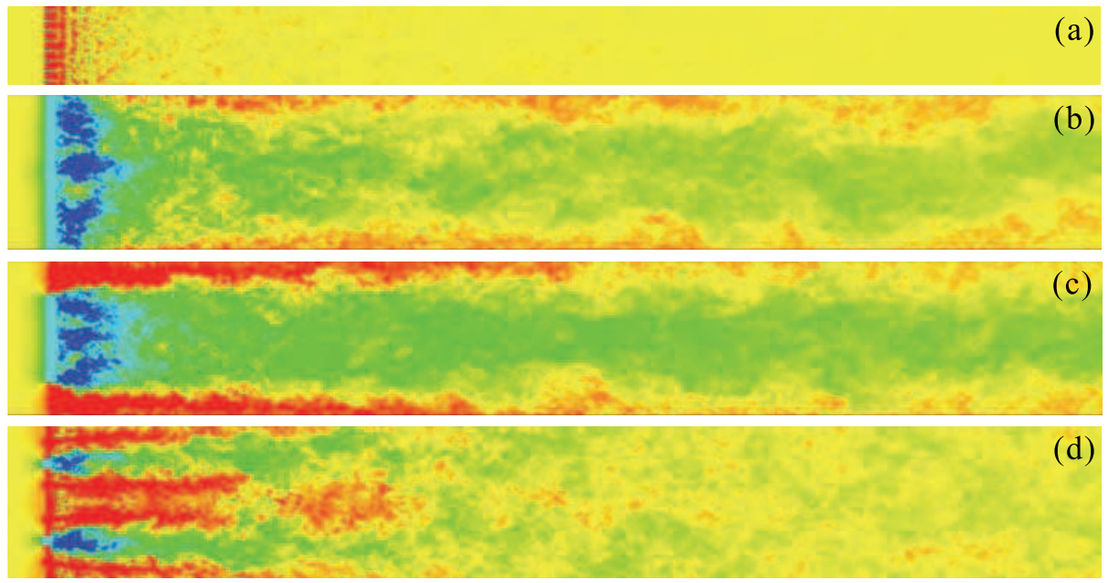
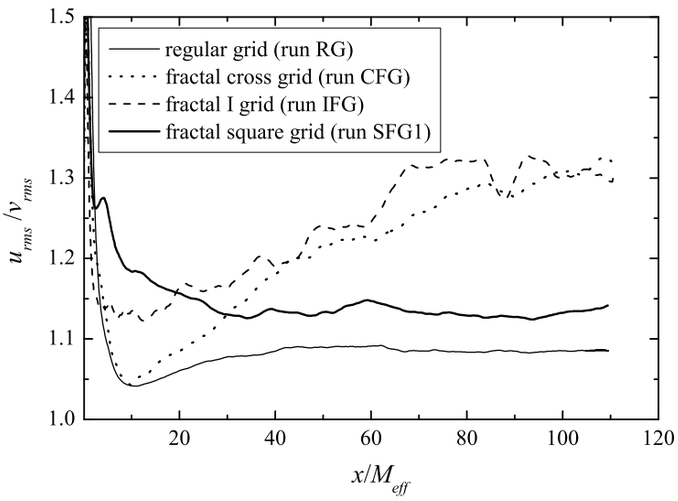
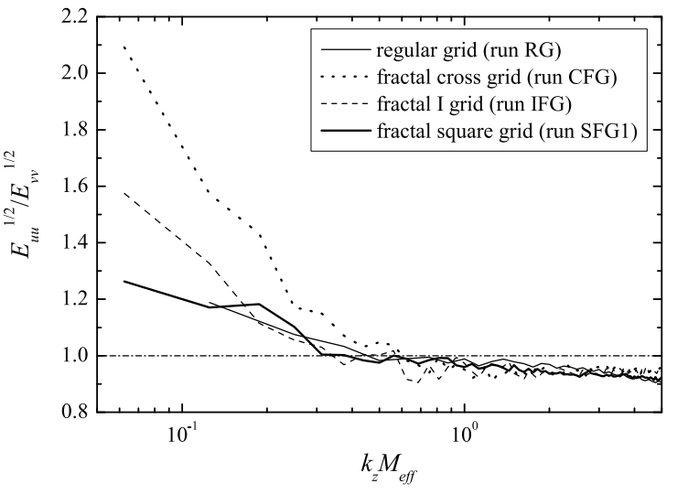


Fig. 14. Instantaneous flow fields downstream of (a) regular grid (run RG1), (b) fractal cross grid (run CFG), (c) fractal I grid (run IFG), and (d) fractal square grid (run SFG1). White: high speed ($U = 1.5$), black: low speed ($U = -1.5$)



(a) Large-scale anisotropy: ratio of u_{rms} and v_{rms}



(b) Small-scale anisotropy: ratio of square-root of spectra of u_{rms} and v_{rms}

Fig. 15. Isotropy of turbulence

$$W_{ij} = \frac{1}{2}\left(\frac{\partial u_j}{\partial x_i} - \frac{\partial u_i}{\partial x_j}\right), \; S_{ij} = \frac{1}{2}\left(\frac{\partial u_j}{\partial x_i} + \frac{\partial u_i}{\partial x_j}\right). \tag{25}$$

It can be observed that the regular and fractal grids are adequately constructed using the present method and that the grid turbulence is generated downstream of the grids.
Figure 14 shows the snapshots of the instantaneous velocity field at $z = 0$ plane. Here, the left side of the figure indicates the upstream. The instantaneous contours of streamwise velocity in the entire computational regions are depicted. It can be observed that all the fractal grids generate high turbulence intensities compared with the regular grid turbulence. It is inferred from Fig. 14 that as compared with the fractal cross and the I grids, the fractal square grid returns the optimal homogeneity in the downstream region: in Figs. 14 (b) and (c) (in case of the fractal cross and I grids), significant velocity defects can be observed near the central region even in the far downstream region. In fact, mean velocity profiles show significant velocity defects even in the far downstream region of the fractal cross and I grids (refer to Nagata et al. 2008 for statistics). Note that periodic boundary conditions are applied to y and z boundaries, and therefore, no effects of side walls on the flow field exist.

3.8.3 Isotropy of turbulence

When grid-generated turbulence is experimentally used in fundamental researches as a way of producing quasi homogeneous isotropic turbulence, the degree of isotropy as well as homogeneity should necessarily be important. To evaluate the isotropy of turbulence, Fig. 15 (a) shows the streamwise profiles of the ratio of rms velocities u_{rms}/v_{rms}, which serves as a measure of large-scale anisotropy. The ratio u_{rms}/w_{rms} is identical to u_{rms}/v_{rms} in the fractal-generated turbulence with the symmetrical fractal cross and square grids, as in the case of the mean velocity profile. Figure 15 (a) shows that acceptable isotropy of $u_{rms}/v_{rms} \sim 1.15$ is attained in the far downstream region of the fractal square grid, whereas large anisotropy is observed in the downstream regions of the fractal cross and I grids. Figure 15 (b) shows the ratio of the spectra, $E_{uu}(k_z)^{1/2}/E_{vv}(k_z)^{1/2}$, where k_z is the spanwise wavenumber. It is found

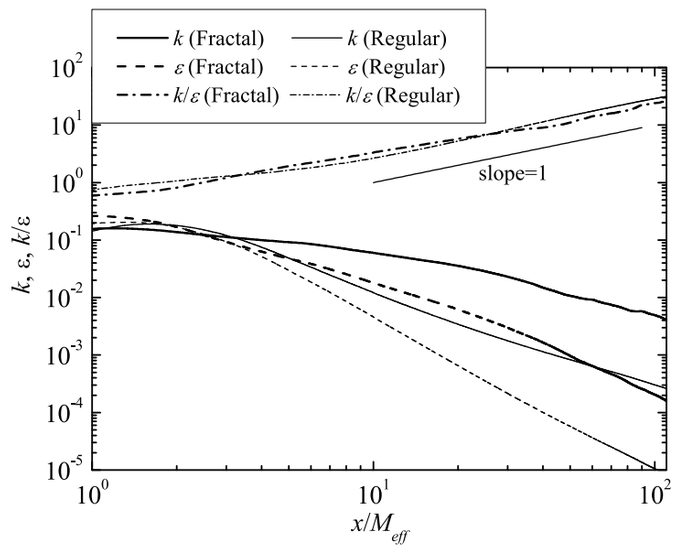


Fig. 16. Streamwise variations of turbulence kinetic energy k, dissipation rate ε, and timescale k/ε downstream of regular and fractal square grids (runs RG1 and SFG1)

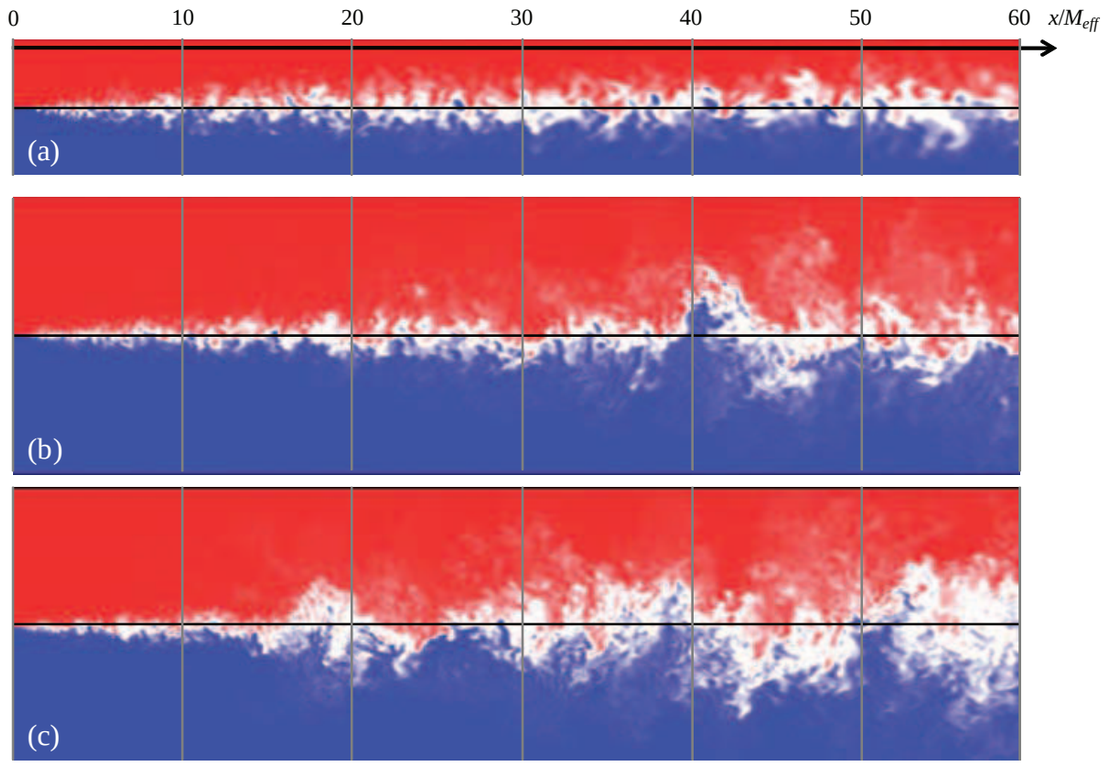


Fig. 17. Instantaneous scalar fields at $z = 0$ in (a) regular grid turbulence (run RGm1), (b) fractal grid turbulence at $t_r = 5.0$ (run SFGm1), and (c) fractal grid turbulence at $t_r = 8.5$ (run SFGm2). In all figures, red: $T = 1$, white: $T = 0.5$, blue: $T = 0$

that the anisotropy of the fractal-generated turbulence with the fractal square grid is mainly due to the anisotropy at a large scale; the acceptable isotropy is attained for fractal-generated turbulence with a fractal square grid in intermediate to smallest scales. The result qualitatively agrees with that of Seoud & Vassilicos (2007). It should be noted that even at the large scale, the anisotropy is less than 1.3 for the fractal square grid; this value is comparable to that in the regular grid turbulence.
The correlation coefficients of the Reynolds stresses (not shown) are small in the downstream region of the fractal square grid, whereas the maximum values are large (approximately 0.5) even in the far downstream regions of the fractal cross and I grids.
The above results suggest that the fractal square grid generates quasi homogeneous isotropic turbulence in the far downstream region of the grid. On the other hand, homogeneous isotropic turbulence could not be generated using the fractal cross and I grids under the present fractal parameters and mesh Reynolds number. Therefore, after this section, we will only show the results for the fractal square grid and regular grid for comparison.

3.8.4 Turbulence statistics

Figure 16 shows the streamwise variations of turbulence kinetic energy $k = \frac{1}{2}\langle u_i u_i \rangle$, dissipation rate ε of k, and timescale of k/ε downstream of regular and fractal square grids (runs RG1 and SFG1, respectively). Here, k and ε are normalized by U_0^2 and U_0^3/M_{eff}, respectively. Note that profiles are averaged over the $y - z$ plane. As shown in previous experiments (Hurst & Vassilicos 2007; Seoud & Vassilicos 2007; Mazellier & Vassilicos 2010;

Suzuki et al. 2010a), k is much larger in the fractal grid turbulence than in the regular grid turbulence. Figure 16 shows that ε is also much larger in the fractal grid turbulence than in the regular grid turbulence. However, the normalized timescale k/ε was almost identical for the regular and fractal grid turbulence. In both flows, the timescale is proportional to x/M_{eff} in the decaying region, which agrees with the relationship derived from the transport equation of k for decaying homogeneous isotropic turbulence, i.e. $dk/dt = -\varepsilon$.
Other turbulence statistics for the flow field downstream of these grids have been shown in Nagata et al. (2008) and Suzuki et al. (2010b).

3.8.5 Scalar fields

Figures 17 and 18 show the instantaneous scalar fields and instantaneous fluctuating scalar fields, respectively, for scalar mixing layers in regular grid turbulence (run RGm1) and fractal grid turbulence (runs SFGm1 and SFGm2) at $z = 0$. The result for run SFGm3 is similar to those for runs SFGm1 and SFGm2 (Suzuki et al. 2009). The interval between the vertical gray lines in Figs. 17 and 18 corresponds to a distance of $10M_{eff}$. Figure 17 shows that the width of the mixing layer is considerably larger for fractal grid turbulence (Figs. 17 (b) and (c)) than for regular grid turbulence (Fig. 17 (a)). In fact, half widths of mean scalar and scalar variance profiles are larger for fractal grid turbulence than for regular grid turbulence (Suzuki et al. 2010c). Thus, as confirmed in our experiment (Suzuki et al. 2010a), for the same Re_M, turbulent mixing is enhanced to a greater extent in the case of fractal grid turbulence than in the case of regular grid turbulence. The fluctuating scalar fields (Fig. 18) also show that

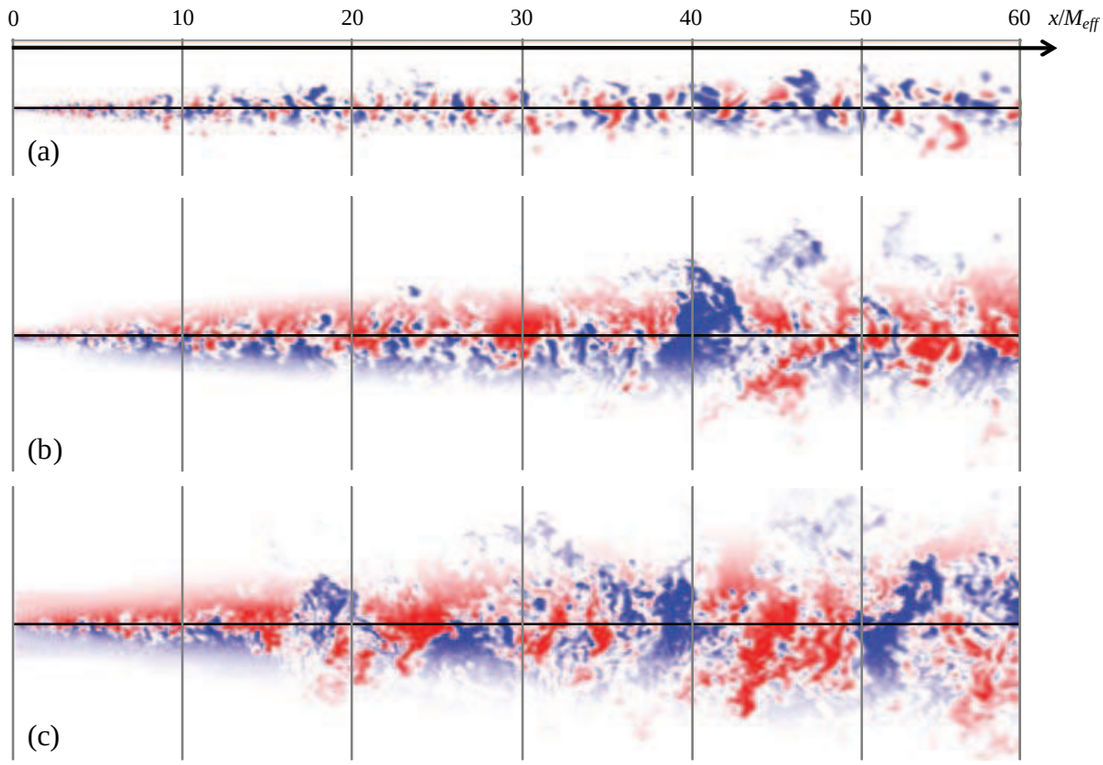


Fig. 18. Instantaneous fluctuating scalar fields at $z = 0$ in (a) regular grid turbulence (run RGm1), (b) fractal grid turbulence at $t_r = 5.0$ (run SFGm1), and (c) fractal grid turbulence at $t_r = 8.5$ (run SFGm2). In all figures, red: $\theta = 0.3$, white: $\theta = 0$, blue: $\theta = -0.3$

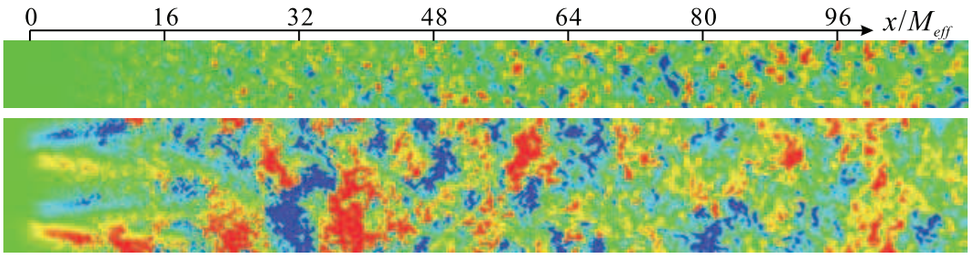


Fig. 19. Instantaneous fluctuating scalar fields at $z = 0$ (with a linear scalar gradient): upper, in regular grid turbulence (run RG1); lower: in fractal grid turbulence (run SFG1)

turbulent mixing is highly enhanced in case of fractal grid turbulence. Further, Figs. 17 and 18 suggest that smaller-scale scalar fluctuations exist in case of fractal grid turbulence.
The intense mixing of scalar can also be found for the linear mean scalar profile (runs RG1 and SFG1), as shown in Fig. 19. Figure 20 shows the streamwise variations of scalar variance $k_\theta = \frac{1}{2}\langle\theta^2\rangle$, scalar dissipation rate ε_θ, and timescale $k_\theta/\varepsilon_\theta$ downstream of the regular and fractal grids with a linear scalar gradient (runs RG1 and SFG1, respectively). k_θ is normalized by ΔT^2, and ε_θ, by $\Delta T^2 U_0/M_{eff}$. The quantities are averaged over the $y-z$ plane. For regular grid turbulence, k_θ increases and ε_θ decreases in the downstream direction after $x/M_{eff} = 3$, while both k_θ and ε_θ decrease in the far downstream region after $x/M_{eff} = 40$ in the fractal grid turbulence. Thus, after $x/M_{eff} = 80$, k_θ becomes larger in the regular grid turbulence than in the fractal grid turbulence. The timescale for scalar fluctuations in the regular grid turbulence is almost identical to k/ε after $x/M_{eff} = 6$, where grid turbulence is fully developed. The term "fully developed" is used here in the context that turbulence intensities have peaks, after which they begin to decay. In contrast, $k_\theta/\varepsilon_\theta$ in the fractal grid turbulence is considerably smaller than that in the regular grid turbulence. It has been shown that the large convection from upstream causes the different behaviors in scalar variance and timescale in the fractal grid turbulence (Nagata et al. 2009).

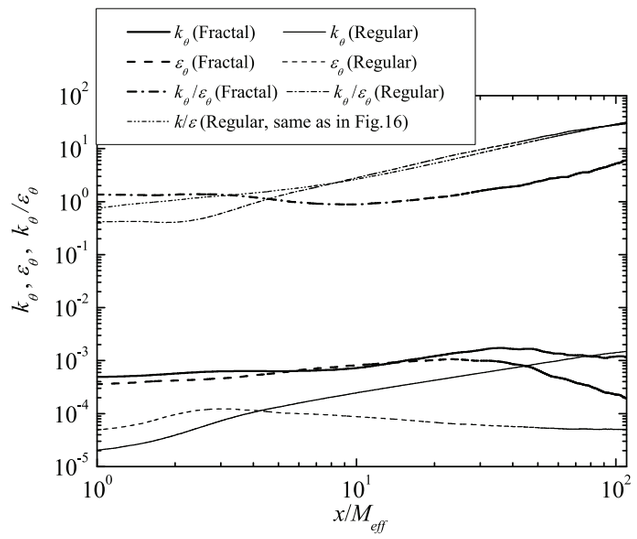


Fig. 20. Streamwise variations of scalar variance k_θ, scalar dissipation rate ε_θ, and timescale $k_\theta/\varepsilon_\theta$ downstream of regular and fractal grids with a linear scalar gradient (runs RG1 and SFG1)

4. Conclusions

A direct numerical simulation (DNS) code was developed for computing turbulent flows with scalar transfer around complex geometries with a spectral-like accuracy. This code is based on the fully conservative higher-order finite-difference schemes for nonlinear terms, the higher-order compact schemes for higher differentiation terms, and the immersed boundary method for numerical building of three-dimensional complex geometries, and is highly optimized for a vector-type supercomputer (NEC SX-8). In the first part of this chapter, we present the results for the canonical channel flow with a scalar transfer obtained using our DNS code and compare them with those obtained using the spectral method. The results show that various turbulence quantities, including spectra, are in excellent agreement with those obtained using the spectral method. Further, our code is applied to turbulent fields with scalar transfer around and downstream of regular and fractal grids as an example of flow around complex geometries. The results show that suitable turbulence and scalar fields are reproduced around and downstream of complex geometries, i.e., regular and fractal grids.
Unfortunately, the application of DNS to complex geometries is currently limited to the moderate Reynolds number and the small Prandtl number ($\sim O(1)$) owing to limitations in computer resources. However, with future advancements in supercomputers, DNS of complex geometry at higher Reynolds numbers and higher Prandtl (or Schmidt) numbers should soon become possible.

5. Acknowledgements

The authors acknowledge Professor J. Christos Vassilicos of Imperial College London and Professor Yohei Morinishi of Nagoya Institute of Technology for providing many valuable comments and suggestions for this study. They also acknowledge Dr. Takashi Kubo (Meijo University) and Mr. Osamu Terashima (Nagoya University) for their help in this study. A part of this study was carried out under the Collaborative Research Project of the Institute of Fluid Science, Tohoku University, and the Research Cooperative Program between the Japan Society for the Promotion of Science and The Royal Society. A part of this study was supported by Grants-in-Aid (Nos. 20008010, 21656051, 22360076, 22360077) from the Japanese Ministry of Education, Culture, Sports, Science and Technology.

6. References

Budwig, R., Tavoularis, S. & Corrsin, S. (1985). Temperature Fluctuations and Heat Flux in Grid-Generated Isotropic Turbulence with Streamwise and Transverse Mean-Temperature Gradients. *Journal of Fluid Mechanics*, Vol. 153, pp. 441-460.

Fadlun, E. A., Verzicco, R., Orlandi, P. & Mohd-Yusof, J. (2000). Combined Immersed-Boundary Finite-Difference Methods for Three-Dimensional Complex Flow Simulations. *Journal of Computational Physics*, Vol. 161, pp. 35-60.

Gad-el-Hak, M. & Morton, J. B. (1979). Experiments on the Diffusion of Smoke in Isotropic Turbulent Flow. *AIAA Journal*, Vol. 17, pp. 558-562.

Gibson, C. H. & Schwarz, W. H. (1963). The Universal Equilibrium Spectra of Turbulent Velocity and Scalar Fields. *Journal of Fluid Mechanics*, Vol. 17, pp. 558-562.

Huq, P. & Britter, R. E. (1995). Mixing Due to Grid-Generated Turbulence of a Two-Layer Scalar Profile. *Journal of Fluid Mechanics*, Vol. 285, pp. 17-40.

Hurst, D. & Vassilicos, J. C. (2007). Scalings and Decay of Fractal-Generated Turbulence. *Physics of Fluids*, Vol. 19, 035103.

Ikeno, T. & Kajishima, T. (2007). Finite-Difference Immersed Boundary Method Consistent with Wall Conditions for Incompressible Turbulent Flow Simulations. *Journal of Computational Physics*, Vol. 226, pp. 1485-1508.

Ito, Y., Nagata, K. & Komori, S. (2002). The Effects of High-Frequency Ultrasound on Turbulent Liquid Mixing with a Rapid Chemical Reaction. *Physics of Fluids*, Vol. 14, pp. 4362-4371.

Iwamoto, K., Suzuki, Y. & Kasagi, N. (2002). Reynolds Number Effect on Wall Turbulence: Toward Effective Feedback Control. *International Journal of Heat and Fluid Flow*, Vol. 23, pp. 678-689.

Jayesh, Yoon, K. & Warhaft, Z. (1991). Turbulent Mixing and Transport in a Thermally Stratified Interfacial Layer in Decaying Grid Turbulence. *Physics of Fluids A*, Vol.3, No.5, pp. 1143-1155.

Kasagi, N., Tomita, Y. & Kuroda, A. (1992). Direct Numerical Simulation of Passive Scalar Field in a Turbulent Channel Flow. *Journal of Heat Transfer*, Vol. 114, pp. 598-606.

Komori, S., Nagata, K., Kanzaki, T. & Murakami, Y. (1993). Measurements of Mass Flux in a Turbulent Liquid Flow with a Chemical Reaction. *AIChE Journal*, Vol. 39, pp. 1611-1620.

Komori, S. & Nagata, K. (1996). Effects of Molecular Diffusivities on Counter-Gradient Scalar and Momentum Transfer in Strongly Stable Stratification. *Journal of Fluid Mechanics*, Vol. 326, pp. 205-237.

Laizet, S. & Vassilicos, J. C. (2010). A Numerical Strategy to Combine High-Order Schemes, Complex Geometry and Parallel Computing for High Resolution DNS of Fractal Generated Turbulence. *Computers & Fluids*, Vol. 39, pp. 471-484.

Lele, S. K. (1992). Compact Finite Difference Schemes with Spectral-Like Resolution. *Journal of Computational Physics*, Vol. 103, pp. 16-42.

Lienhard V, J. H. & Van Atta, C. W. (1990). The Decay of Turbulence in Thermally Stratified Flow. *Journal of Fluid Mechanics*, Vol. 210, pp. 57-112.

Mazellier, N. & Vassilicos, J. C. (2010). Turbulence without Richardson-Kolmogorov Cascade. *Physics of Fluids*, Vol. 22, 075101.

Morinishi, Y., Lund, T. S., Vasilyev, O. V. & Moin, P. (1998). Fully Conservative Higher Order Finite Difference Schemes for Incompressible Flow. *Journal of Computational Physics*, Vol. 143, pp. 90-124.

Nagata, K. & Komori, S. (2000). The Effects of Unstable Stratification and Mean Shear on the Chemical Reaction in Grid Turbulence. *Journal of Fluid Mechanics*, Vol. 408, pp. 39-52.

Nagata, K. & Komori, S. (2001). The Difference in Turbulent Diffusion between Active and Passive Scalars in Stable Thermal Stratification. *Journal of Fluid Mechanics*, Vol. 430, pp. 361-380.

Nagata, K., Wong, H., Hunt, J. C. R., Sajjadi, S. G. & Davidson, P. A. (2006). Weak Mean Flows Induced by Anisotropic Turbulence Impinging onto Planar and Undulating Surfaces. *Journal of Fluid Mechanics*, Vol. 556, pp. 329-360.

Nagata, K., Suzuki, H., Sakai, Y., Hayase, T. & Kubo, T. (2008). Direct Numerical Simulation of Turbulence Characteristics Generated by Fractal Grids. *International Review of Physics*, Vol. 2, pp. 400-409.

Nagata, K., Suzuki, H., Sakai Y. & Hayase, T. (2009). Turbulence Structure and Scalar Transfer in Fractal Generated Turbulence. *Proceedings of Japan-Korea CFD Workshop*, CD-ROM.

Nagata, K., Hunt, J. C. R., Sakai, Y. & Wong, H. (2010). Distorted Turbulence and Secondary Flow near Right Angled Plates. *Journal of Fluid Mechanics*, in press.

Nakamura, I., Sakai, Y. & Miyata, M. (1987). Diffusion of Matter by a Non-Buoyant Plume in Grid-Generated Turbulence. *Journal of Fluid Mechanics*, Vol. 178, pp. 379-403.

Proud, O., Fincham, A. M. & Sommeria, J. (2005). Decaying Grid Turbulence in a Strongly Stratified Fluid. *Journal of Fluid Mechanics*, Vol. 522, pp. 1-33.

Seoud, R. E. & Vassilicos, J. C. (2007). Dissipation and Decay of Fractal-Generated Turbulence. *Physics of Fluids*, Vol. 19, 105108.

Sreenivasan, K. R., Tavoularis, S., Henry, R. & Corrsin, S. (1980). Temperature Fluctuations and Scales in Grid-Generated Turbulence. *Journal of Fluid Mechanics*, Vol. 100, pp. 597-621.

Stapountzis, H., Sawford, B. L., Hunt, J. C. R. & Britter, R. E. (1986). Structure of the Temperature Field Downwind of a Line Source in Grid Turbulence. *Journal of Fluid Mechanics*, Vol. 165, pp. 401-424.

Stillinger, D. C., Helland, K. N. & Van Atta, C. W. (1983). Experiments on the Transition of Homogeneous Turbulence to Internal Waves in a Stratified Fluid. *Journal of Fluid Mechanics*, Vol. 131, pp. 91-122.

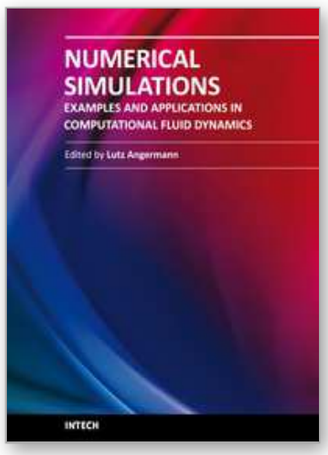
Suzuki, H., Nagata, K., Sakai, Y., Hayase, T. & Kubo, T. (2009). DNS of Passive Scalar Field with Mean Gradient in Fractal-Generated Turbulence. *Proceedings of 6th International Symposium on Turbulence and Shear Flow Phenomena*, Vol. 1, pp. 55-60.

Suzuki, H., Nagata, K., Sakai, Y. & Ukai, R. (2010a). High Schmidt Number Scalar Transfer in Regular and Fractal Grid Turbulence. *Physica Scripta*, in press.

Suzuki, H., Nagata, K., Sakai, Y. & Hayase, T. (2010b). Direct Numerical Simulation of Regular and Fractal-Grid Turbulence Using the Immersed Boundary Method and Fully Conservative Higher-Order Finite-Difference Schemes. *International Review of Physics*, Vol. 4, No. 2, pp. 83-90.

Suzuki, H., Nagata, K., Sakai, Y. & Hayase, T. (2010c). Direct Numerical Simulation of Turbulent Mixing in Regular and Fractal Grid Turbulence. *Physica Scripta*, in press.

Warhaft, Z. & Lumley, J. L. (1978). An Experimental Study of the Decay of Temperature Fluctuations in Grid-Generated Turbulence. *Journal of Fluid Mechanics*, Vol. 88, pp. 659-684.



Numerical Simulations - Examples and Applications in Computational Fluid Dynamics

Edited by Prof. Lutz Angermann

ISBN 978-953-307-153-4
Hard cover, 440 pages
Publisher InTech
Published online 30, November, 2010
Published in print edition November, 2010

This book will interest researchers, scientists, engineers and graduate students in many disciplines, who make use of mathematical modeling and computer simulation. Although it represents only a small sample of the research activity on numerical simulations, the book will certainly serve as a valuable tool for researchers interested in getting involved in this multidisciplinary ï¬eld. It will be useful to encourage further experimental and theoretical researches in the above mentioned areas of numerical simulation.

How to reference

In order to correctly reference this scholarly work, feel free to copy and paste the following:

Kouji Nagata, Hiroki Suzuki, Yasuhiko Sakai and Toshiyuki Hayase (2010). Direct Numerical Simulation of Turbulence with Scalar Transfer around Complex Geometries Using the Immersed Boundary Method and Fully Conservative Higher-Order Finite-Difference Schemes, Numerical Simulations - Examples and Applications in Computational Fluid Dynamics, Prof. Lutz Angermann (Ed.), ISBN: 978-953-307-153-4, InTech, Available from: http://www.intechopen.com/books/numerical-simulations-examples-and-applications-in-computational-fluid-dynamics/direct-numerical-simulation-of-turbulence-with-scalar-transfer-around-complex-geometries-using-the-i

INTECH
open science | open minds

InTech Europe
University Campus STeP Ri
Slavka Krautzeka 83/A
51000 Rijeka, Croatia
Phone: +385 (51) 770 447
Fax: +385 (51) 686 166
www.intechopen.com

InTech China
Unit 405, Office Block, Hotel Equatorial Shanghai
No.65, Yan An Road (West), Shanghai, 200040, China
中国上海市延安西路65号上海国际贵都大饭店办公楼405单元
Phone: +86-21-62489820
Fax: +86-21-62489821

© 2010 The Author(s). Licensee IntechOpen. This chapter is distributed under the terms of the Creative Commons Attribution-NonCommercial-ShareAlike-3.0 License, which permits use, distribution and reproduction for non-commercial purposes, provided the original is properly cited and derivative works building on this content are distributed under the same license.

IntechOpen

IntechOpen